

1                   **Statistical characteristics of raindrop size**  
2                   **distribution during rainy seasons in Complicated**  
3                   **Mountain Terrain**

4                   Wenqian Mao<sup>1,3,4</sup>, Wenyu Zhang<sup>2,3,4</sup>, Menggang Kou<sup>2</sup>

- 5                   1. College of Resources and Environmental Sciences, Gansu Agricultural University, Lanzhou  
6                   730070, China  
7                   2. School of Geoscience and Technology, Zhengzhou University, Zhengzhou, 450001, China  
8                   3. Key Laboratory for Cloud Physics, Chinese Academy of Meteorological Sciences, Beijing  
9                   100081, China  
10                  4. College of Atmospheric Sciences, Lanzhou University, Lanzhou, 730000, China

11                  Correspondence to: Wenqian Mao (mdycmwq@163.com)

12                  **Abstract:** In order to improve understanding of the characteristics of raindrop size  
13                  distribution (DSD) over complex mountainous terrain, the differences in DSD over the  
14                  southern slopes, northern slopes and interior of the Qilian Mountains were analyzed  
15                  using six months of observations. For all rainfall events, the number concentrations of  
16                  small and large raindrops in the interior and on the southern slopes were greater than  
17                  on the northern slopes, but midsize raindrops were less. The DSD spectrum of the  
18                  interior was more variable and differed significantly from that of the northern slopes.  
19                  The differences in the normalized intercept parameters of the DSD for stratiform and  
20                  convective rainfall were 8.3% and 10.4%, respectively, and those of the mass-weighted  
21                  mean diameters were 10.0% and 23.4%, respectively, while the standard deviations of  
22                  DSD parameters at interior sites were larger. The differences in the coefficient and  
23                  exponent of the Z-R relationship were 2.5% and 10.7%, respectively, with an increasing  
24                  value of the coefficient from the southern to the northern slopes for stratiform rainfall,  
25                  but the opposite for convective rainfall. In addition, the DSD characteristics and Z-R  
26                  relationships were more similar at the ipsilateral sites and had smaller differences  
27                  between the southern slopes and interior of the mountains.

28  
29                  **Keywords:** raindrop size distribution; complicated mountain terrain; spatial variation  
30

## 31 1 Introduction

32 Raindrop size distribution (DSD), the number of raindrops per drop size per unit  
33 volume, is an important parameter to statistically describe the microstructure of  
34 precipitation (Bringi et al., 2003; Ma et al., 2019a). The measurement of DSD can  
35 provide some fundamental information such as raindrop size ( $D$ ), liquid water content  
36 ( $W$ ), rain rate ( $R$ ), radar reflectivity factor ( $Z$ ) and so on, which has an essential  
37 contribution to improving quantitative precipitation estimation (QPE) using weather  
38 radar and satellite observations (Adirosi et al., 2018; Jash et al., 2019). The  
39 parameterization of DSD can obtain the distribution model parameters of DSD in  
40 different rain types, which is significant in advancing microphysics parameterization in  
41 numerical weather prediction (NWP) models (Wainwright et al., 2014; McFarquhar et  
42 al., 2015; Zhao et al., 2019). In addition, understanding the DSD is crucial in many  
43 applied fields concerning hydrology, agriculture, soil erosion and microwave  
44 communication (Rincon et al., 2002; Smith et al., 2009; Angulo-Martínez et al., 2015;  
45 Lim et al., 2015; Yang et al., 2016).

46 Numerous studies have been carried out on the statistical characteristics of DSD  
47 in different regions (Campos et al., 2006; Seela et al., 2017; Dolan et al., 2018; Protat  
48 et al., 2019; Loh et al., 2019; Jash et al., 2019). It has been shown that the number  
49 concentration and size of raindrops increase with rain rate and so the DSD becomes  
50 higher and wider. The characteristics in different rain types demonstrate that the mass-  
51 weighted mean diameter (i.e.,  $D_m$ ) and normalized intercept parameter (i.e.,  $N_w$ ) of  
52 convective rainfall are larger than those of stratiform rainfall. Furthermore, these  
53 studies also reveal that there are more differences in the characteristics of DSD. Dolan  
54 et al. (2018) divided global DSD characteristics into 6 types by using 12 datasets across  
55 three latitudes and found that the centralized regions and DSD parameters of the 6 types  
56 varied in location. The average number of raindrops in central Korea was usually  
57 greater than that in the southeast under three rainfall systems, especially drops in the  
58 0.31–0.81mm diameter range (Loh et al., 2019). According to DSD measurements in  
59 the Tibetan Plateau region, eastern areas have a higher raindrop number concentration  
60 in the diameter range of 0.437–1.625 mm and greater variation in diameters than in  
61 central areas (Wang et al., 2020). Compared to eastern China and northern China, the  
62 DSD in southern China shows a higher number concentration of relatively small-sized  
63 drops (Zhang et al., 2019). Comparison of the  $Z$ - $R$  relationship (defined as  $Z=AR^b$ )  
64 indicates that the coefficient decreases with increasing  $R$  in the southern Tibetan Plateau,  
65 which is opposite to the case in southern China (Wu et al., 2017). For the DSD  
66 parameters of stratiform and convective rainfall, there are various changes between the  
67 lower and middle reaches of the Yangtze River (Fu et al., 2020).

68 As reported in the above studies, DSD characteristics vary significantly with  
69 factors such as geographical location, climatic region and rain types. Pu et al. (2020)  
70 analyzed the DSD characteristics of five sites in Nanjing city and found the  $N_w$  of DSD  
71 to be largest at site near industrial areas, but the  $D_m$  of DSD was largest at sites near the  
72 city's center. In other words, even at the urban scale, there are still differences in the  
73 microphysical characteristics reflected by the DSD, which is due to the influence of the  
74 surrounding environment. How, then, do the characteristics of DSD vary from location

75 to location over the complicated mountain terrain? Rao et al. (2006), by comparing the  
76 DSD parameters at different altitudes, suggested that the obvious variation in DSD with  
77 altitude is related to the processes of evaporation and breakup. Using aircraft  
78 observations, Geoffroy et al. (2014) concluded that the total concentration of raindrops  
79 decreased while the average drop size increased with decreasing altitude. But how large  
80 might the differences in DSD be at different altitudes in mountainous regions? And how  
81 significant might the effects be of these differences?

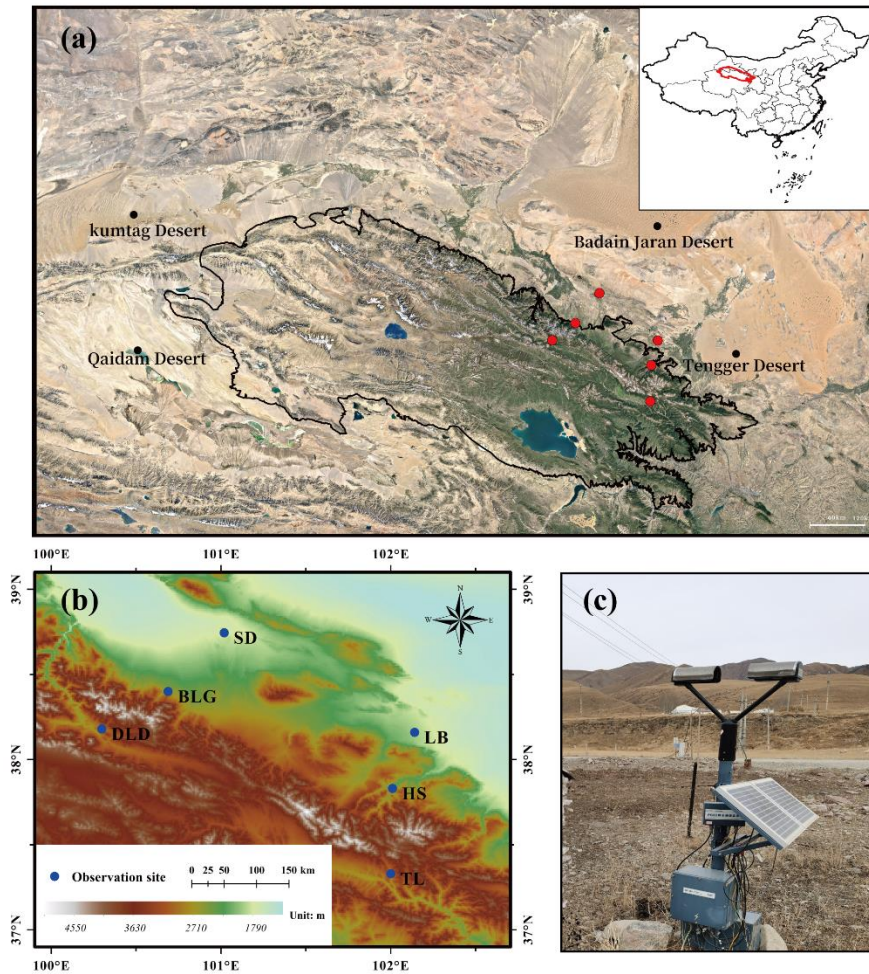
82 The Qilian Mountains, a series of marginal mountains in the northeastern part of  
83 the Tibetan Plateau, are a vitally important ecological protection barrier in the northwest  
84 arid areas of the region, that block the connection between deserts and wilderness  
85 ( Figure 1a). The mountains form several inland rivers that are important water sources  
86 for the arid areas of the northwest and have therefore made a considerable contribution  
87 to regional economic development (Gou et al., 2005; Tian et al., 2014; Qin et al., 2016).  
88 In this study, we chose the Qilian Mountains as the research object and selected six sites  
89 with different backgrounds representing the southern slopes, northern slopes and  
90 interior of the mountains. To thoroughly investigate the discrepancies in this complex  
91 mountain terrain, the DSD characteristics and *Z-R* relationships were comprehensively  
92 analyzed according to different rain types based on continuous disdrometer  
93 observations in the rainy season. The primary goal was to obtain a deeper understanding  
94 and characteristic differences of DSD over the Qilian Mountains and refine the accuracy  
95 of QPE, which could then be used as a research foundation for developing cloud water  
96 resources in mountainous areas.

## 97 **2 Data and method**

### 98 **2.1 Sites and instruments**

99 The eastern and middle sections of the Qilian Mountains were chosen as the main  
100 study area, taking into account that several important inland rivers originate from these  
101 areas (Li et al., 2019). Six disdrometers were deployed on the southern slopes, northern  
102 slopes and interior (close to the ridge) of the Qilian Mountains, with three sites in the  
103 eastern section [called Taola (TL), Huangchengshuiguan (HS) and Liuba (LB), from  
104 south to north] and another three sites in the middle section [called Daladong (DLD),  
105 Boligou (BLG) and Shandan (SD), from south to north]. The background of the Qilian  
106 Mountains is shown on the satellite map in Figure 1a, and the six sites are marked on  
107 the topographical map, also in Figure 1b. The distances between the six sites are listed  
108 in Table 1. The sites in the south, north and interior are basically parallel to the  
109 orientation of the mountains, and the sections formed by the sites in the east and interior  
110 are basically perpendicular to it. On the basis of an historical weather review and rain  
111 gauge observations, the rainy season at the six sites is concentrated in May to October,  
112 with more precipitation in July, August and September.

113



114  
 115 Figure 1. (a) Geographical overview of the Qian Mountains; (b) the disdrometer sites  
 116 (circles); (c) the observation device at TL site. Source: Google Earth © Google Earth  
 117 YEAR

118 Table 1. Site details (latitude, longitude, sea level height) and distances (km) between  
 119 pairs of sites.

Six sites	LB	HS	TL	SD	BLG	DLD
LB (38.16°N, 102.14°E, 1926m)	-	39.6	94.3	116.0	129.6	161.1
HS (37.83°N, 102.01°E, 2342m)	-	-	55.6	135.1	132.8	154.9
TL (37.33°N, 102.00°E, 2910m)	-	-	-	182.4	167.3	177.0
SD (38.80°N, 101.08°E, 1765m)	-	-	-	-	54.2	96.8
BLG (38.4°N, 100.69°E, 2455m)	-	-	-	-	-	43.3
DLD (38.18°N, 100.3°E, 2957m)	-	-	-	-	-	-

120 This study used an optical, laser-based device to measure the DSD, called a DSG4  
 121 disdrometer (Figure 1c), which meets the Functional Specification Requirements for  
 122 Disdrometer issued by the China Meteorological Administration. This disdrometer has  
 123 an HSC-OTT Parsivel2 sensor as the observation part, manufactured by OTT  
 124 Messtechnik (Germany) and Huatron (China). When raindrops pass through the  
 125 horizontal flat laser beam generated by the transmitting part of the instrument, it causes

126 signal attenuation in the laser observation area. The raindrop size is determined by the  
 127 degree of signal attenuation and the falling speed is recorded by the transit time. The  
 128 sampling time is 60s and the velocity and drop sizes are divided into 32 non-equally  
 129 spaced bins, varying from 0.05 to 20.8 m s<sup>-1</sup> for velocity and 0.062 to 24.5 mm for drop  
 130 diameter.

## 131 2.2 Quality control of the data

132 It was necessary to quality control the data because of potential instrument error.  
 133 Every minute of DSD data collected by the six DSG4 disdrometers from May to  
 134 October 2020 was carefully processed. Specifically, the following criteria were  
 135 employed in choosing data for analysis(Jaffrain et al., 2011; Guyot et al., 2019; Pu et  
 136 al., 2020): (1) the first two size bins were ignored because of low signal-to-noise ratio;  
 137 (2) samples with 1-min total of raindrop number less than 10, or a rain rate at the  
 138 moment of discontinuous observation less than 0.1 mmh<sup>-1</sup> were regarded as noise  
 139 (corresponds to the second sample in Table 2); (3) raindrops with diameters more than  
 140 8 mm were eliminated; (4) raindrops with a falling terminal velocity  $V(D_i)$  that deviated  
 141 from the empirical terminal velocity  $V_{emp}(D_i)$  by more than 40% were removed (Kruger  
 142 and Krajewski, 2002); and (5) samples with less than five bins after the correction of  
 143 falling terminal velocity were deleted because their DSDs could not be determined with  
 144 too few bins. The fourth criterion can be expressed by the formula:

$$145 \quad |V(D_i) - V_{emp}(D_i)| < 0.4V_{emp}(D_i) \quad (1)$$

146 where  $V_{emp}(D_i) = 9.65 - 10.3\exp(-0.6D_i)$  ( $D_i$  is the mean volume-equivalent  
 147 diameter of the  $i$ th size category), as derived from the formula given in Atlas et al.  
 148 (1973).

149 After data quality control, the sample statistics of key steps are shown in Table 2.  
 150 The number of 1-min DSD spectra selected from the six sites (LB, HS, TL, SD, BLG,  
 151 DLD) after data quality control covering the rainy season (May–October) in the Qilian  
 152 Mountains region in 2020 were 11103, 17619, 14814, 10736, 18861 and 13230,  
 153 respectively, which accounted for 87.9%, 85.8%, 84.5%, 91.2%, 80.6% and 86.5% of  
 154 the total number of samples.

155 Table 2. Sample statistics of data quality control at six sites

Samples	LB	HS	TL	SD	BLG	DLD
Total minutes (min)	12625	20536	17526	11770	23401	15289
Total minutes without noise (min)	12602	20509	17494	11756	23371	15267
After quality control (min)	11103	17619	14814	10736	18861	13230
Available data (%)	87.9%	85.8%	84.5%	91.2%	80.6%	86.5%

156

## 157 2.3 Integral parameters of rainfall

158 The basic observations obtained by the disdrometer were the counts of raindrops  
 159 at each diameter and velocity. Also, the diameters given by the disdrometers were the  
 160 mid value of two adjacent bins, which we take as the corresponding endpoint bin values.  
 161 The velocities were the weighted average velocity class over the corresponding

162 disdrometer. The raindrop number concentration  $N(D_i)$  ( $\text{m}^{-3} \text{mm}^{-1}$ ) in the  $i$ th size bin  
 163 per unit volume per unit size interval for diameter was calculated by the following  
 164 equation:

$$165 \quad N(D_i) = \sum_{i,j=1}^{32} \frac{n_{i,j}}{A \cdot \Delta t \cdot V_j \cdot \Delta D_i} \quad (2)$$

166 where  $n_{i,j}$  denotes the counts of raindrops measured by the disdrometer within size bin  
 167  $i$  and velocity bin  $j$  during the sampling time  $\Delta t$ ;  $A$  and  $\Delta t$  are the sampling area ( $0.0054$   
 168  $\text{m}^2$ ) and sampling time ( $60$  s), respectively;  $V_j$  ( $\text{m s}^{-1}$ ) is the mid-value falling speed for  
 169 velocity bin  $j$ ; and  $\Delta D_i$  is the diameter spread for the  $i$ th diameter bin.

170 Some integral rainfall parameters, such as the total number concentration  $N_t$  ( $\text{m}^{-3}$ ),  
 171 rain rate  $R$  ( $\text{mm h}^{-1}$ ), radar reflectivity factor  $Z$  ( $\text{mm}^6 \text{m}^{-3}$ ) and liquid water content  $W$   
 172 ( $\text{g cm}^{-3}$ ), can be derived by the following equations:

$$173 \quad N_t = \sum_{i=1}^{32} N(D_i) \Delta D \quad (3)$$

$$174 \quad R = \frac{6\pi}{10^4 \rho_w} \sum_{i=1}^{32} V(D_i) D_i^3 N(D_i) \Delta D_j \quad (4)$$

$$175 \quad Z = \sum_{i=1}^{32} N(D_i) D_i^6 \Delta D_i \quad (5)$$

$$176 \quad W = \frac{\pi \rho_w}{6 \times 10^3} \sum_{i=1}^{32} D_i^3 N(D_i) \Delta D_i \quad (6)$$

177 where  $\rho_w$  is the water density ( $1.0 \text{ gcm}^{-3}$ ); and  $V(D_i)$  is the falling speed from the  
 178 disdrometer. In this study, when calculating the rain rate we use  $V_{emp}(D_i)$  to replace  $V(D_i)$   
 179 because of measurement error, particularly at larger bins and faster falling speeds,  
 180 which is inspired from Tokay et al. (2014) and Zhang et al. (2019).

181 The characteristics of DSD can be described by a three-parameter gamma  
 182 distribution in the form introduced by Ulbrich (1983). Also, it has better fitting  
 183 capability than the M-P distribution on the broader variation of DSD fluctuations,  
 184 including the middle rain drops, especially on small and large rain scales. The three-  
 185 parameter gamma distribution can be expressed by the following formula:

$$186 \quad N(D) = N_0 D^\mu \exp(-\Lambda D) \quad (7)$$

187 where  $N(D)$  is the raindrop number concentration;  $D$  is the raindrop bins with unit  $\text{mm}$ ;  
 188 and  $N_0$ ,  $\mu$  and  $\Lambda$  are the intercept, shape and slope parameter from the three parameters  
 189 of the gamma model, which can be derived from gamma moments or the least-squares  
 190 method, respectively. When  $\mu=0$ , it degenerates into the M-P DSD model.

191 Although, the gamma distribution is commonly accepted, the normalized gamma  
 192 distribution has also been widely adopted with its independent parameters and clear  
 193 physical meaning as follows (Dolan et al., 2018; Ma et al., 2019):

$$194 \quad N(D) = \frac{3}{128} N_w \left[ \frac{(4 + \mu)^{(4+\mu)}}{\Gamma(4 + \mu)} \right] \left( \frac{D}{D_m} \right)^\mu \exp\left( -\frac{(4 + \mu)D}{D_m} \right) \quad (8)$$

195 where  $\mu$  is the shape parameter, which is in dimensionless;  $D_m$  (mm) is the mass-  
 196 weighted mean diameter, and  $N_w$  ( $\text{m}^{-3} \text{mm}^{-1}$ ) is the normalized intercept parameter  
 197 computed from  $D_m$ . The form is as follows:

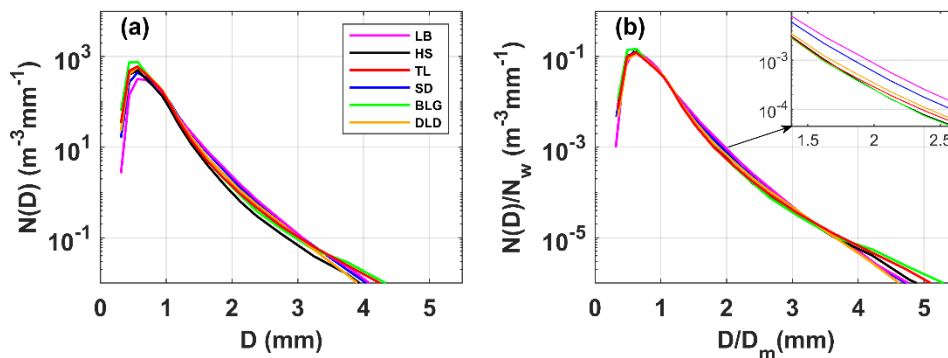
$$198 \quad D_m = \frac{\sum_{i=1}^{32} N(D_i) D_i^4 \Delta D_i}{\sum_{i=1}^{32} N(D_i) D_i^3 \Delta D_i} \quad (9)$$

$$199 \quad N_w = \frac{4^4}{\pi \rho_w} \left( \frac{10^3 W}{D_m^4} \right) \quad (10)$$

### 200 3 DSD parameter characteristics

#### 201 3.1 Characteristics of DSD

202 Figure 2a shows the mean DSDs for the six sites during the rainy season in the  
 203 Qilian Mountains. The maximum concentration of raindrops was around 0.562 mm in  
 204 diameter and the maximum number concentration values of sites were order as follows:  
 205 BLG>TL>DLD>HS>SD>LB. As the diameter increased, the number concentration  
 206 decreased and the concentration values followed the order  
 207 LB>SD>DLD>TL>BLG>HS at around 2 mm in diameter. When the diameter was  
 208 larger than 4 mm, the concentration at TL, BLG and HS was relatively high. In this  
 209 study, the data were roughly divided into small raindrops (less than 1 mm in diameter),  
 210 midsize raindrops (1–3 mm) and large raindrops (greater than 3 mm) to easily describe  
 211 the difference in DSDs (Ma et al., 2019b; Pu et al., 2020). To highlight the DSD  
 212 differences caused by the background environment, Figure 2b shows the mean DSDs  
 213 normalized by the  $N_w$  and  $D_m$  results for the sites. Compared with Figure 2a, the  
 214 raindrop characteristics were more consistent across sizes, while the differences  
 215 between the sites were more pronounced, especially in the midsize and large raindrops,  
 216 which truly reflected the DSD differences caused by the location. Combining the  
 217 characteristics of the geographical environment of the six sites, we can analyze some  
 218 differences in DSD characteristics in the Qilian Mountains. For small raindrops, the  
 219 number concentrations at interior and southern-slope sites were greater than at northern-  
 220 slope sites; for midsize raindrops, the number concentrations decreased sequentially at  
 221 the northern-slope, southern-slope and interior sites; and for large raindrops, the number  
 222 concentrations at the interior sites were larger. In addition, the number concentrations  
 223 of raindrops in the middle section of this the mountainous area were slightly greater  
 224 than those in the eastern section.

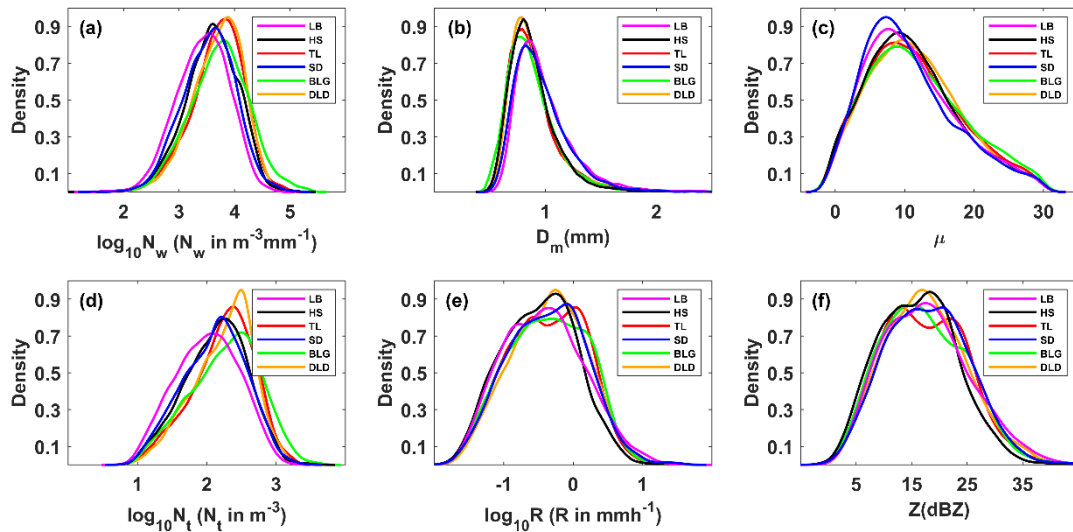


225

226 Figure 2. The (a) mean and (b) normalized mean DSDs at six sites in the Qilian  
 227 Mountains region in the rainy season

### 228 3.2 Distribution of DSD parameters

229 In order to study the differences in DSDs, we selected six integral rainfall  
 230 parameters for discussion—namely, the normalized intercept parameter ( $N_w$ ), mass-  
 231 weighted mean diameter ( $D_m$ ), shape parameter ( $\mu$ ), total number concentration ( $N_t$ ),  
 232 rain rate ( $R$ ) and radar reflectivity factor ( $Z$ ). Figure 3 and Table 3 show the distributions  
 233 and statistics of these six DSD parameters (the distribution of each was normalized  
 234 using the uniform method). On average,  $D_m$  was more concentrated on smaller values  
 235 at HS and BLG, which showed smaller mean values than TL and DLD but significantly  
 236 more values greater than 1 mm at LB and SD;  $\log_{10}N_w$  was more centralized on larger  
 237 values at TL and DLD, with relatively smaller values at LB and SD; and the distribution  
 238 patterns for  $\mu$  and  $\log_{10}N_t$  were similar to those for  $\log_{10}N_w$ . The density curves of  $R$  and  
 239  $Z$  were similar, but there were differences among the six sites, which are analyzed in  
 240 detail later in the paper. It is noteworthy that the frequency of samples with  $R$  around  
 241 0.6–1.0 mm h<sup>-1</sup> was highest, and samples with  $R$  less than 1mm h<sup>-1</sup> accounted for more  
 242 than half of the total rainfall.  
 243



244  
 245 Figure 3. Probability density distribution of integral DSD parameters at six sites (LB,  
 246 HS, TL, SD, BLG, DLD): (a) normalized intercept parameter  $\log_{10}N_w$  ( $N_w$  in  $\text{m}^{-3}\text{mm}^{-1}$ );  
 247 (b) mass-weighted mean diameter  $D_m$  (mm); (c) shape parameter  $\mu$ ; (d) total number  
 248 concentration  $\log_{10}N_t$  ( $N_t$  in  $\text{m}^{-3}$ ); (e) rain rate  $\log_{10}R$  ( $R$  in  $\text{mm h}^{-1}$ ); (f) radar reflectivity  
 249 factor  $Z$  (dBZ)

250 Table 3. Statistical of several integral DSD parameters for all observations at six sites  
 251 (LB, HS, TL, SD, BLG, DLD).

Sites	$\log_{10}N_w$			$D_m$			$\mu$			$\log_{10}N_t$			$R$			$Z$		
	ME	SD	SK	ME	SD	SK	ME	SD	SK	ME	SD	SK	ME	SD	SK	ME	SD	SK
LB	3.43	0.47	-0.25	0.99	0.29	2.68	10.92	6.63	0.61	2.01	0.46	-0.07	0.94	1.90	0.23	17.79	7.82	0.44



HS	3.59	0.48	-0.29	0.89	0.25	3.35	11.12	6.64	0.53	2.13	0.45	-0.22	0.69	1.60	0.05	16.24	7.08	0.34
TL	3.69	0.48	-0.55	0.90	0.29	4.49	11.37	6.84	0.48	2.23	0.44	-0.43	0.89	1.48	-0.05	17.47	7.55	0.35
SD	3.54	0.48	-0.17	0.96	0.26	2.12	10.62	6.61	0.71	2.11	0.46	-0.17	0.97	2.01	0.06	17.95	7.47	0.28
BLG	3.72	0.54	-0.15	0.89	0.29	5.17	11.71	7.06	0.46	2.26	0.50	-0.25	0.94	2.13	-0.04	17.34	7.66	0.41
DLD	3.69	0.45	-0.50	0.90	0.25	2.66	11.52	6.66	0.43	2.24	0.43	-0.46	0.95	1.62	-0.01	17.70	7.43	0.37

252 Note: ME is mean; SD is standard deviation; SK is skewness.

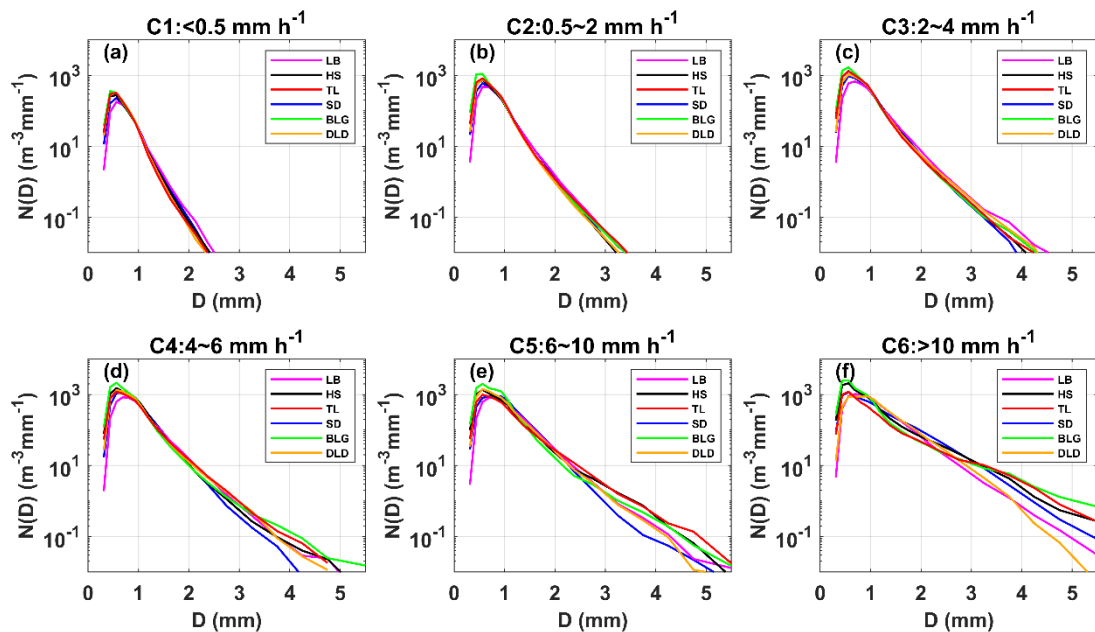
### 253 3.3 DSD characteristics in different rain rate classes

254 To further understand the characteristics of DSDs at the six sites, the samples were  
255 divided into six classes according to the associated rain rates ( $R$ ): C1,  $R < 0.5$ ; C2,  
256  $0.5 \leq R < 2$ ; C3,  $2 \leq R < 4$ ; C4,  $4 \leq R < 6$ ; C5,  $6 \leq R < 10$ ; C6,  $R \geq 10$  mm h<sup>-1</sup>. This classification  
257 was based on two considerations: firstly, the number of observation samples in different  
258 rainfall rates roughly conformed to a normal distribution; and secondly, the mean  
259 maximum diameter interval of different rainfall rates gradually increased (Li et al.,  
260 2019). Of course, other classification studies were referenced and the fact that the rain  
261 rate in this area is smaller than that in southern China was taken into account (Ma et al.,  
262 2019b; Zeng et al., 2021). Figure 4 shows the mean DSDs at each rainfall rate class for  
263 the six sites. Table 4 lists the number of samples and statistical values of the DSD  
264 parameters for the six classes. Clearly, as the rainfall rate increased, the number  
265 concentration of almost all raindrop sizes and the width of DSD shapes increased, and  
266 thus the tail of the DSD shape moved gradually towards a larger diameter, similar to  
267 previous findings, such as those of Ma et al. (2019b) and Pu et al. (2020). Taking a  
268 number concentration of 0.01 m<sup>-3</sup>mm<sup>-1</sup>, the mean maximum diameter of DSD in each  
269 class was ordered as follows: 2.3–2.5, 3.2–3.4, 3.9–4.5, 4.3–5.0, 5.0–5.6 and 6.0–7.0  
270 mm (the sixth-class diameter range is not fully shown in the figure). In class C1, the  
271 number concentrations were relatively similar at different sites; starting from class C2,  
272 the differences in number concentration increased when the diameter was greater than  
273 2 mm for the six sites; and the differences of in number concentration were gradually  
274 reflected in each raindrop size bin as the rainfall rate class increased. Observationally,  
275 the DSDs of BLG, HS and TL had larger number concentrations in different rainfall  
276 rate classes, and the DSD parameters and standard deviations (SDs) were larger,  
277 especially for BLG.

278 Table 4. Statistics of several integral DSD parameters for six rain rate classes at six sites.

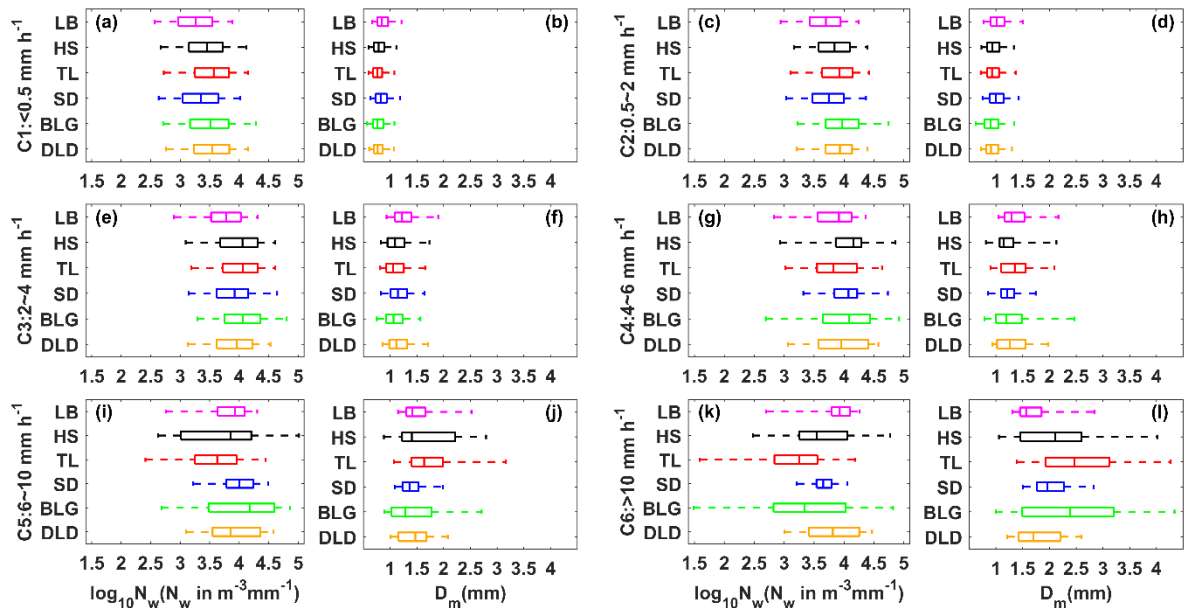
Class	Sites	Samples	$\log_{10}N_w$		$D_m$		$\mu$		$\log_{10}N_t$		$R$		$Z$	
			ME	SD	ME	SD	ME	SD	ME	SD	ME	SD	ME	SD
C1(<0.5 mm h <sup>-1</sup> )	LB	6520	3.25	0.41	0.88	0.18	12.36	7.09	1.74	0.34	0.20	0.13	12.68	4.52
	HS	10753	3.43	0.44	0.81	0.17	12.01	7.03	1.89	0.37	0.20	0.13	11.90	4.54
	TL	7858	3.52	0.44	0.79	0.16	12.91	7.12	1.96	0.37	0.20	0.13	11.78	4.16
	SD	5772	3.34	0.43	0.85	0.18	11.72	6.99	1.82	0.36	0.20	0.13	12.51	4.40
	BLG	10073	3.50	0.48	0.79	0.17	12.94	7.28	1.94	0.40	0.20	0.13	11.73	4.26
	DLD	6891	3.51	0.43	0.79	0.15	13.04	6.92	1.96	0.36	0.21	0.13	12.14	4.15
C2(0.5~2 mm h <sup>-1</sup> )	LB	3318	3.66	0.41	1.06	0.24	9.93	5.75	2.30	0.28	1.00	0.41	22.55	3.27
	HS	5700	3.82	0.39	0.97	0.21	10.21	5.88	2.44	0.26	0.96	0.37	21.67	3.09

	TL	5368	3.87	0.42	0.98	0.23	10.35	6.15	2.49	0.26	1.07	0.41	22.18	3.33
	SD	3778	3.73	0.41	1.03	0.23	9.94	6.14	2.36	0.28	1.02	0.40	22.40	3.15
	BLG	6411	3.97	0.47	0.94	0.25	11.24	6.72	2.56	0.30	1.07	0.43	21.69	3.69
	DLD	4778	3.88	0.37	0.95	0.20	10.91	6.02	2.47	0.24	1.01	0.40	21.60	3.19
	LB	782	3.71	0.47	1.31	0.37	7.33	4.28	2.52	0.29	2.77	0.56	29.54	2.87
	HS	884	3.96	0.50	1.16	0.34	8.42	5.22	2.73	0.27	2.76	0.54	28.33	3.06
C3(2~4 mm h <sup>-1</sup> )	TL	1232	4.00	0.47	1.13	0.33	8.70	5.93	2.75	0.23	2.68	0.53	28.07	3.16
	SD	812	3.89	0.44	1.19	0.27	8.57	5.53	2.63	0.26	2.71	0.53	28.41	2.68
	BLG	1865	4.05	0.49	1.11	0.30	8.62	5.75	2.81	0.25	2.70	0.53	27.99	3.29
	DLD	1111	3.91	0.44	1.18	0.29	7.81	5.45	2.70	0.23	2.74	0.54	28.73	3.09
	LB	229	3.80	0.47	1.41	0.40	7.33	3.94	2.65	0.31	4.76	0.57	32.69	2.63
	HS	191	4.03	0.54	1.28	0.47	7.54	4.42	2.86	0.27	4.80	0.56	31.70	3.34
C4(4~6 mm h <sup>-1</sup> )	TL	213	3.84	0.56	1.41	0.51	6.23	4.64	2.77	0.28	4.77	0.54	32.82	3.54
	SD	187	4.03	0.41	1.24	0.27	8.35	5.02	2.80	0.22	4.76	0.54	31.32	2.52
	BLG	321	3.99	0.66	1.33	0.53	7.97	6.10	2.93	0.27	4.78	0.54	32.44	4.40
	DLD	270	3.92	0.53	1.35	0.47	6.50	4.80	2.83	0.25	4.83	0.56	32.55	3.47
	LB	167	3.81	0.46	1.55	0.44	6.46	3.38	2.72	0.27	7.66	1.22	35.74	2.85
	HS	49	3.69	0.74	1.70	0.68	6.89	4.82	2.75	0.38	7.42	1.09	36.14	4.29
C5(6~10 mm h <sup>-1</sup> )	TL	103	3.57	0.62	1.78	0.66	5.20	4.62	2.71	0.32	7.32	1.02	37.03	3.76
	SD	128	3.96	0.39	1.42	0.35	7.10	3.96	2.82	0.21	7.68	1.17	34.76	2.42
	BLG	138	3.97	0.76	1.51	0.80	8.34	6.35	2.99	0.27	7.37	1.02	35.09	4.96
	DLD	122	3.90	0.46	1.46	0.34	6.13	4.20	2.86	0.26	7.29	1.11	35.32	2.88
	LB	87	3.85	0.44	1.73	0.53	5.08	3.05	2.87	0.32	14.81	7.57	39.58	3.57
	HS	42	3.60	0.65	2.19	0.92	6.74	5.27	3.00	0.28	21.69	9.91	42.93	6.11
C6(>10 mm h <sup>-1</sup> )	TL	40	3.16	0.69	2.69	1.19	4.34	5.20	2.74	0.32	18.25	9.69	44.70	5.41
	SD	59	3.66	0.29	2.04	0.46	3.30	2.48	2.91	0.16	21.07	8.34	42.85	4.10
	BLG	53	3.38	0.93	2.58	1.52	5.58	6.19	3.00	0.37	21.95	9.05	44.08	7.50
	DLD	58	3.82	0.47	1.80	0.46	6.64	4.12	2.84	0.28	16.58	7.21	40.13	3.53



280 Figure 4. Distribution of mean measured DSD for different rain rate classes at six sites.

281 Figure 5 shows box-and-whisker plots of the normalized intercept parameter  
 282  $\log_{10}N_w$  and mass-weighted mean diameter  $D_m$  for six sites in each rain rate class. The  
 283 middle line in the box indicates the median. The left and right lines indicate the 25<sup>th</sup> and  
 284 75<sup>th</sup> percentiles. The left and right ends of whiskers indicate the most extreme data  
 285 points between the 5<sup>th</sup> and 95<sup>th</sup> percentiles, except outliers. The median  $D_m$  gradually  
 286 increased with a larger value range as the rain rate class increased, particularly for HS  
 287 and BLG in class C5 and C6. The median  $\log_{10}N_w$  increased in class C1 to C3 and then  
 288 tended to decrease in class C5 to C6, for which the reduction was obvious at sites with  
 289 a larger value range, such as HS and BLG. Ma et al. (2019b) also obtained similar  
 290 conclusions that  $D_m$  values increase with the increased rainfall intensity, while the  
 291  $\log_{10}N_w$  is not as clear. The indication was that the increase in rain rate was mainly due  
 292 to the growth in raindrop size. Also, the change in number concentration may have been  
 293 caused by the imbalance between the loss of number concentration at small raindrop  
 294 size and the addition at large raindrop sizes, which in a sense implies a relationship  
 295 between the collision–coalescence and break–up of raindrops. It is worth noting that  
 296 the microphysical processes were quite different among the sites, being greatly  
 297 influenced by the surrounding environment. Because HS and BLG were located in the  
 298 interior of the mountains and close to the ridge, their dynamics and thermodynamics as  
 299 well underlying surfaces were thus different from those of other sites.

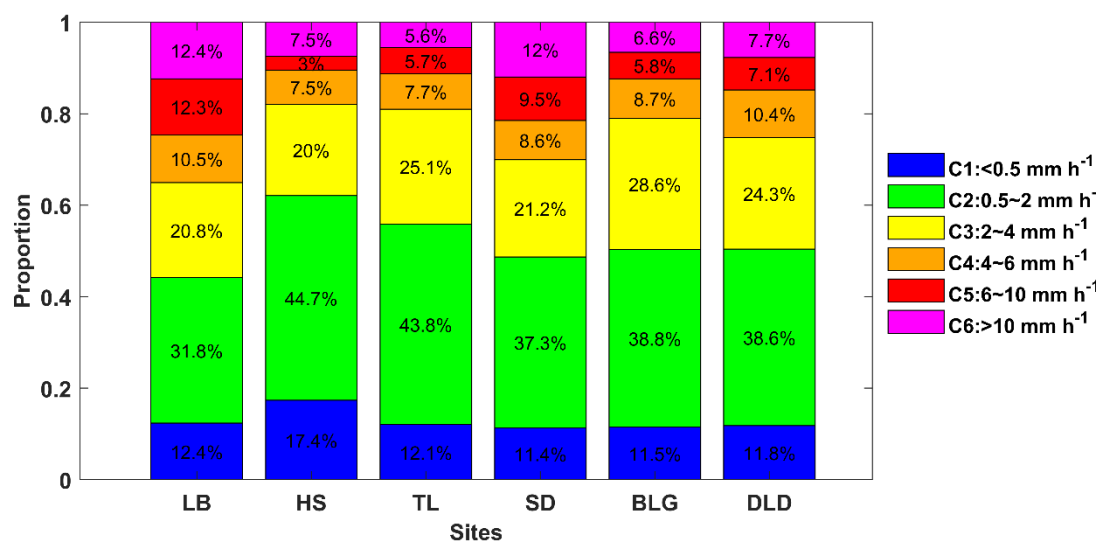


300

301 Figure 5. Variation of the normalized intercept parameter  $\log_{10}N_w$  (a) and the mass-  
 302 weighted mean diameter  $D_m$  (b) for different rain rate classes at six sites. The three lines  
 303 in the boxes are the 25<sup>th</sup>, 50<sup>th</sup> and 75<sup>th</sup> percentiles, from left to right, respectively. The  
 304 whiskers at the left and right ends are the 5<sup>th</sup> and 95<sup>th</sup> percentiles, respectively. The  
 305 colors represent the six sites as in other figures.

306 Figure 6 displays the contribution of different rain rate classes to the total rainfall  
 307 at different sites. It is clear that C2 contributed the most to the total rainfall of all sites,

308 followed by C3, and the sum of the two classes' contribution could reach 60% of the  
 309 total rainfall. Compared with the interior and southern-slope sites, C2 and C3  
 310 contributed slightly less to sites LB and SD (i.e., the northern slopes), while C5 and C6  
 311 contributed relatively more to sites LB and SD, indicating that there is a greater  
 312 probability of heavy precipitation events on the northern slopes. The DSD parameters  
 313 in Table 3 provide a more detailed representation of the rainfall differences between the  
 314 three geographical sections of the Qilian Mountains, i.e., the interior, southern slopes  
 315 and northern slopes. Meanwhile, it also reflects the characteristics of rainfall in the  
 316 eastern and interior sections, such as the eastern section had larger  $Z$  and  $D_m$  and smaller  
 317  $\log_{10}N_w$  and  $\log_{10}N_t$  compared to the interior. It is possible that there is a certain spatial  
 318 connection between precipitation at the sites, related to factors such as the source of  
 319 precipitation vapor, weather system and so on.



320

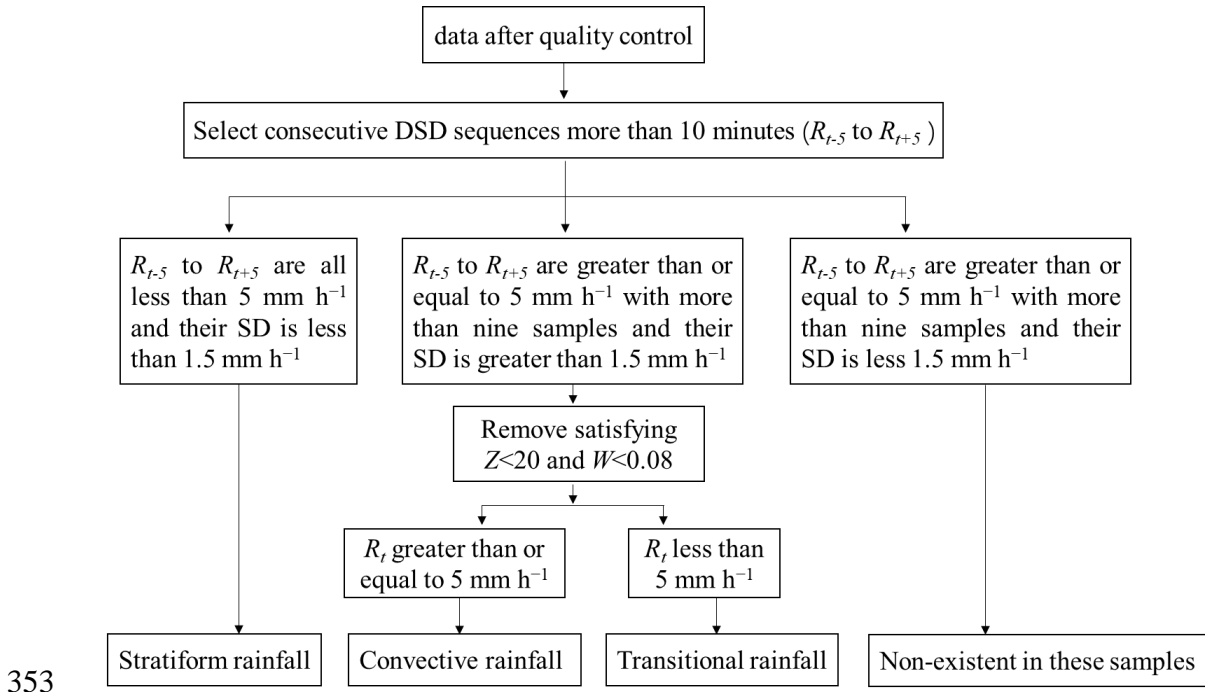
321 Figure 6. Proportion of rainfall with different rain rate classes to rain amount at six sites.

### 322 3.4 DSD properties for different rain types

323 Previous studies on DSD have shown that there are significant differences in the  
 324 DSD of convective and stratiform rainfall in the same climatic region, which has a  
 325 substantial impact on the parameterization of NWP and remote sensing observations  
 326 (Bringi et al., 2003; Penide et al., 2013). Due to the different physical mechanisms of  
 327 convective and stratiform rainfall, it is possible to discuss the differences in  
 328 microphysical structures for rainfall types through their DSD. Studies have employed  
 329 many different classification methods for rainfall types; example, Testud et al. (2001)  
 330 used the rain rate; Chen et al. (2013) combined the rain rate and its SD; and the findings  
 331 of Das et al. (2018) were based on the rain rate and radar reflectivity factor. Among  
 332 these, the method of Chen et al. (2013) has commonly been used to establish samples  
 333 of convective and stratiform rainfall, but mainly in semi-humid or humid regions with  
 334 relatively high rain rate and rainfall. However, the Qilian Mountains are located in the  
 335 semi-arid regions of China and far from the sea, where the average rainfall rain and  
 336 rainfall are quite different from in semi-humid regions. Therefore, this paper proposes  
 337 a new classification method for precipitation applicable to the arid and semi-arid

338 regions of Northwest China based on the classification ideas of Chen et al. (2013) and  
 339 Das et al. (2018).

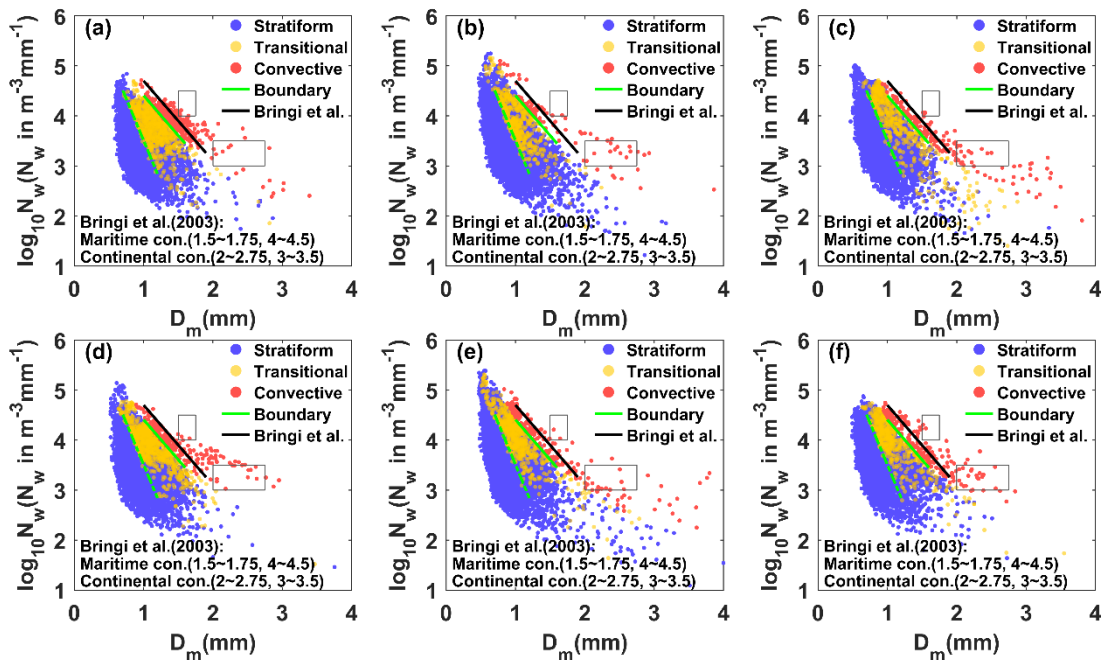
340 Firstly, the sequences of DSD with continuous 1-min samples more than 10 min  
 341 are determined, and  $R_t$  is defined as the rain rate at time  $t$ . In the first case, the  $R$   
 342 of samples from  $R_{t-5}$  to  $R_{t+5}$  are all less than  $5 \text{ mm h}^{-1}$  and their SD is less than  $1.5 \text{ mm}$   
 343  $\text{h}^{-1}$ ; in the second case, the  $R$  of samples from  $R_{t-5}$  to  $R_{t+5}$  are greater than or equal to  $5$   
 344  $\text{mm h}^{-1}$  with more than nine samples and their SD is greater than  $1.5 \text{ mm h}^{-1}$ ; and in  
 345 the third case, the situation is the same as the second case but their SD is less  $1.5 \text{ mm}$   
 346  $\text{h}^{-1}$ . Secondly, samples satisfying  $Z < 20$  and  $W < 0.08$  in the second case are removed  
 347 (Thurai et al., 2016; Das et al., 2018). And then, samples with  $R_t$  greater than or equal  
 348 to  $5 \text{ mm h}^{-1}$  in the second case are regarded as convective rainfall and samples with  $R_t$   
 349 less than  $5 \text{ mm h}^{-1}$  in the second case are regarded as transitional rainfall (the rainfall  
 350 stage in which convective precipitation develops and declines). Samples in the first case  
 351 are regarded as stratiform rainfall. Through experiments, the third case does not exist.  
 352 The main calculation process is shown in Figure 7



354 Figure 7. Classification method for rainfall types in the Qilian Mountains.

355 The  $\log_{10}N_w$  and  $D_m$  of different rainfall types were different, which were taken as  
 356 the main research objects. Figure 8 shows the variation of  $\log_{10}N_w$  with  $D_m$  at different  
 357 sites. The blue, red and yellow scatter points represent stratiform, convective and  
 358 transitional rainfall, respectively. Obviously, there are fairly clear boundaries between  
 359 the scatter points for the different precipitation type events, and the same dividing line  
 360 can be used to distinguish between the different rainfall types at different sites. The  
 361 green solid lines were drawn based on visual examination of the data with a slope of  
 362 approximately  $-1.60$  and intercept of  $6.008$  to represent the split between stratiform,  
 363 transitional and convective rainfall in all subplots. The green dashed line can distinguish  
 364 transitional rainfall (transitional and stratiform rainfall have an overlap area) with a

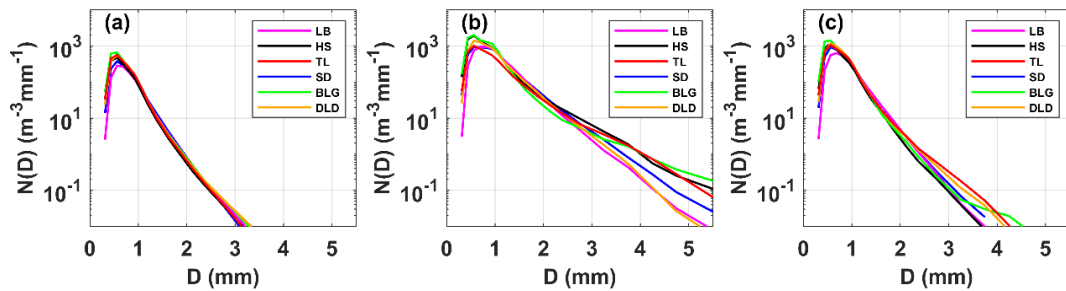
365 slope of approximately  $-3.338$  and intercept of  $6.847$ . Note that the dividing line  
 366 between stratiform and convective rainfall has the same slope as that obtained by Bringi  
 367 et al. (2003) (solid green line with a slope of  $-1.6$  and intercept of  $6.3$ ), who fitted  
 368 composite results based on disdrometer data and from radar retrievals covering many  
 369 climate conditions from near the equator to plateau. The  $\log_{10}N_w$  and  $D_m$  from the  
 370 figures for stratiform, convective and transitional rainfall are respectively concentrated  
 371 in the ranges of  $3.1\text{--}3.9$ ,  $0.75\text{--}1.1$  mm;  $3.8\text{--}4.2$ ,  $1.4\text{--}1.6$  mm;  $3.6\text{--}4.0$ ,  $1.05\text{--}1.2$  mm.  
 372 Compared to the maritime-like cluster and continental-like cluster of convective rainfall  
 373 proposed by Bringi et al. (2003), the convective events in the Qilian Mountains are not  
 374 belong to continental-like cluster or maritime-like cluster, while the averages of  $D_m$  are  
 375 slightly less than the continental-like cluster and the averages of  $\log_{10}N_w$  are greater  
 376 than the continental-like cluster. There are isolated convective events in the maritime-  
 377 like cluster, but it is difficult to consistent with the features of the geographical location  
 378 of the Qilian Mountains.  
 379



380  
 381 Figure 8. Scatter plot of  $\log_{10}N_w$  versus  $D_m$  for different rain types at (a) LB, (b) HS, (c)  
 382 TL, (d)SD, (e)BLG, and (f)DLD. The stratiform cases, convective cases and transitional  
 383 cases are represented by blue, red and yellow scatter points, respectively. The green  
 384 dashed lines are the  $\log_{10}N_w\text{--}D_m$  relationship for stratiform versus convective cases and  
 385 stratiform versus transitional case. The black dashed lines are the  $\log_{10}N_w\text{--}D_m$   
 386 relationship for stratiform versus convective cases and stratiform versus transitional  
 387 case from Bringi et al. (2003). The green dotted lines are the area of overlap between  
 388 stratiform and transitional case.

389 Figure 9 shows the mean DSDs for stratiform, convective and transitional rainfall  
 390 at the six sites. The range of number concentrations and corresponding raindrop  
 391 diameters for the three types were significantly different, matching the basic  
 392 characteristics of DSD. The mean DSDs of stratiform rainfall differed slightly among

393 the sites; convective rainfall had big differences at among the sites; and transitional  
 394 rainfall presented more differences beginning at larger than 2.2 mm in diameter, which  
 395 were the expected results. Stratiform rainfall usually has a large horizontal extent and  
 396 an homogeneous cloud distribution, which makes the DSD characteristics basically the  
 397 same under the influence of the same cloud system in mountainous areas. However,  
 398 convective rainfall is related to local thermal and dynamical factors, which could lead  
 399 to differences in DSD at different sites when considering the complex topography and  
 400 diverse underlying surfaces in mountainous areas. For example, for convective rainfall,  
 401 there was a significant increase in the number concentration of raindrops larger than 2.2  
 402 mm in diameter at BLG, HS and TL, indicating that these sites are conducive to the  
 403 development of convective precipitation. Also, the number concentration of small  
 404 raindrops at BLG and HS were higher than at TL (the southern slope), which may be  
 405 due to the higher altitude of the interior sites reducing the falling distance of raindrops  
 406 after exiting the cloud and decreasing the impact of collision on the raindrop evolution.  
 407 In other words, even for the same rainfall type, the microphysics of rainfall at different  
 408 sites is still different, depending on the topography and position of the observation point  
 409 relative to the cloud base.



410

411 Figure 9. Distribution of mean measured DSD for (a) stratiform rainfall, (b) convective  
 412 rainfall and (c) transitional rainfall at six sites.

413 Figure 10 shows box-and-whisker plots of  $\log_{10}N_w$  and  $D_m$  for different rain types.  
 414 The  $\log_{10}N_w$  and  $D_m$  of stratiform rainfall were smaller than those of convective rainfall  
 415 but larger than those of transitional rainfall. Sites with a large  $\log_{10}N_w$  value range had  
 416 larger value ranges for  $D_m$ ; and sites with a large median  $\log_{10}N_w$  had a smaller median  
 417  $D_m$ , especially at sites HS and BLG for convective rainfall. Based on the mean values  
 418 of the six sites in Table 5, the DSD characteristics in the Qilian Mountains consist of a  
 419 larger  $N_w$  and smaller  $D_m$  (compared the results of studies in other regions, seeing  
 420 discussion section for details) due to the melting of tiny, compact graupel, and rimed  
 421 ice particles (relative to large, low-density snowflakes). Compared with transitional  
 422 rainfall, the  $D_m$  of convective rainfall was obviously larger, indicating that the increase  
 423 in rain rate in this area is mainly due to the growth in raindrop size. Moreover, on the  
 424 northern slopes one should consider the increase in number concentration, because the  
 425  $\log_{10}N_w$  of convective rainfall also increased. Note that the number of convective  
 426 samples on the northern slopes was higher than that of other sites, which corresponds  
 427 to the speculation regarding the contribution of different rain rate classes. On average,  
 428 for stratiform rainfall, the dispersion degree of  $\log_{10}N_w$  and  $D_m$  at different sites was  
 429 8.3% and 10.0%, respectively; and for convective rainfall it was 10.4% and 23.4%. The

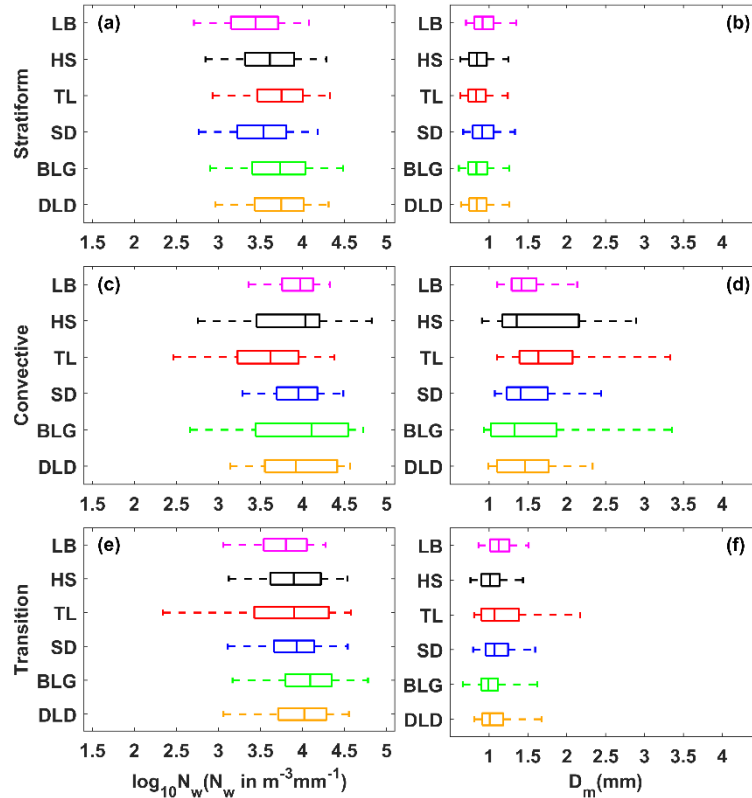
430 SDs of DSD parameters at sites HS and BLG were relatively large.

431 Table 5 Statistics of several integral DSD parameters for six sites with stratiform rainfall,  
 432 convective rainfall and transitional rainfall

Type	Sites	Number	$\log_{10}N_w$		$D_m$		$\mu$		$\log_{10}N_t$		$R$		$Z$	
			ME	SD	ME	SD	ME	SD	ME	SD	ME	SD	ME	SD
S	LB	7123	3.42	0.42	0.96	0.21	11.48	7.98	1.98	0.38	0.54	0.60	16.93	5.93
	HS	12694	3.60	0.44	0.88	0.21	11.24	7.89	2.14	0.40	0.54	0.58	16.17	6.06
	TL	10091	3.71	0.43	0.87	0.20	11.90	8.01	2.23	0.39	0.65	0.67	16.85	6.15
	SD	7175	3.51	0.44	0.95	0.22	11.15	8.03	2.07	0.39	0.62	0.64	17.36	6.10
	BLG	12467	3.72	0.49	0.88	0.23	12.24	8.50	2.25	0.44	0.70	0.74	17.11	6.33
	DLD	9685	3.70	0.42	0.88	0.21	11.91	7.91	2.23	0.38	0.67	0.69	17.18	6.13
C	LB	292	3.91	0.35	1.49	0.35	6.50	3.30	2.81	0.23	9.28	5.56	35.88	3.59
	HS	100	3.85	0.67	1.71	0.84	6.33	4.33	2.95	0.30	12.55	13.75	37.32	6.64
	TL	159	3.54	0.59	1.87	0.74	5.21	4.97	2.72	0.30	9.48	6.91	37.96	5.21
	SD	219	3.91	0.37	1.54	0.47	6.61	4.68	2.85	0.19	10.75	7.68	36.24	5.02
	BLG	198	3.91	0.74	1.64	0.97	8.00	7.37	3.00	0.27	10.57	15.49	36.29	6.75
	DLD	203	3.94	0.48	1.50	0.43	6.96	5.24	2.87	0.27	9.41	6.04	35.89	4.27
T	LB	787	3.76	0.39	1.15	0.21	8.37	4.35	2.47	0.31	2.16	1.25	26.42	3.89
	HS	541	3.89	0.49	1.05	0.29	8.98	6.74	2.59	0.33	1.81	1.15	24.79	3.89
	TL	465	3.77	0.70	1.22	0.49	8.81	6.91	2.56	0.44	2.30	1.21	27.10	4.39
	SD	819	3.87	0.41	1.12	0.26	8.23	5.46	2.59	0.28	2.28	1.18	26.59	4.04
	BLG	665	4.04	0.51	1.04	0.31	10.33	7.31	2.72	0.33	2.19	1.13	25.66	4.44
	DLD	503	3.95	0.46	1.10	0.30	8.69	6.16	2.67	0.31	2.35	1.17	26.60	4.20

433





434  
435

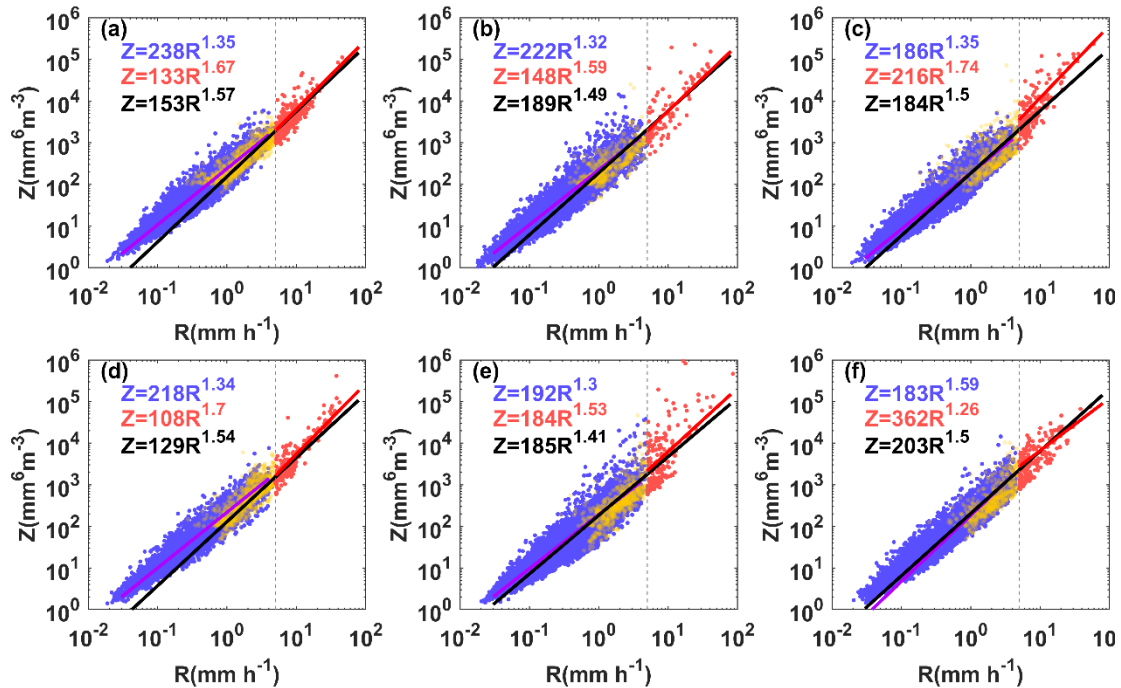
Figure 10. As in Fig. 5 but for different rain types at six sites.

### 436 3.5 Implications for radar rainfall estimation with DSD

437 The sixth moment of raindrop diameter is proportional to the radar reflectivity  
 438 factor and the 3.76th moment is approximately the rain rate (they can be calculated by  
 439 Equations 4 and 5). Generally, the theoretical basis of QPE for single polarization radar  
 440 (ground-based or space-based) is the power relationship between the radar reflectivity  
 441 and rainfall rate ( $Z=AR^b$ ). This makes the coefficients  $A$  and exponents  $b$  of the power  
 442 relationship heavily dependent on the variation in DSD. Therefore, it is necessary to  
 443 obtain the  $A$  and  $b$  of different sites according to different rainfall types.

444 Figure 11 shows the  $Z$ - $R$  scatter plots for different sites and the fitted power-law  
 445 relationships for different rainfall types. The blue and red scatter points represent  
 446 stratiform and convective rainfall, respectively. The purple, red and black solid lines  
 447 indicate the  $Z$ - $R$  relationships for stratiform, convective and total rainfall, respectively.  
 448 It shows that the  $Z$ - $R$  scatter points for HS and BLG were relatively scattered around  
 449 the  $5 \text{ mm h}^{-1}$  rain rate. Besides, the  $Z$ - $R$  relationship of total rainfall underestimated the  
 450 stratiform rainfall at low  $R$  values and the convective rainfall at high  $R$  values. Based  
 451 on the average  $Z$ - $R$  relationship using a least-squares method, the dispersion degree of  
 452  $A$  and  $b$  at different sites was 42.5% and 10.7%, respectively, which reveals there to be  
 453 large differences in mountain areas.

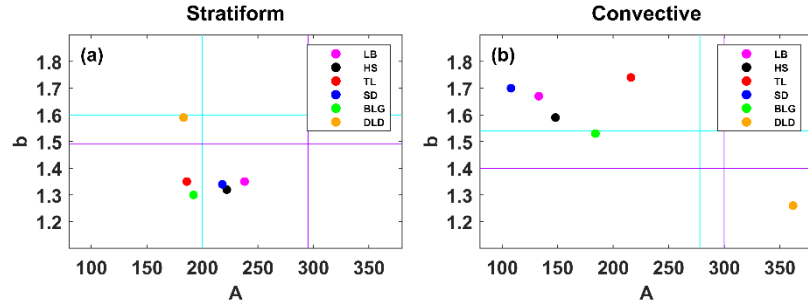
454



455

456 Figure 11. Scatter plots of  $Z$  ( $\text{mm}^6 \text{m}^{-3}$ ) versus  $R$  ( $\text{mm h}^{-1}$ ) for three rain types at (a) LB,  
 457 (b) HS, (c) TL, (d)SD, (e)BLG, and (f)DLD. The blue, red and yellow scatter points,  
 458 represent stratiform, convective and transitional cases, respectively. The purple, red and  
 459 black lines denote the  $Z$ - $R$  relations. The blue, red and black formula denote stratiform,  
 460 convective and total  $Z$ - $R$  relationships. The grey dashed line indicates  $r$  is  $5 \text{ mmh}^{-1}$

461 In order to compare the six sites  $Z$ - $R$  relationships with some standard  $Z$ - $R$   
 462 relationships, the results for  $Z=300R^{1.4}$  for convective rainfall commonly used in radar,  
 463 and  $Z=200R^{1.6}$  (i.e., M48) for stratiform rainfall commonly used in midlatitude areas,  
 464 are provided in Figure 12. Overall, convective rainfall had smaller values of  $A$  and  
 465 larger values of  $b$  than those of stratiform rainfall (excluding DLD). The  $A$  values of  
 466 convective rainfall were smaller than the commonly used  $Z$ - $R$  relationship with large  
 467 differences, but the  $b$  values were greater. The distribution of  $A$  and  $b$  for stratiform  
 468 rainfall was relatively concentrated, with  $A$  and  $b$  ranging from 186–238 and 1.3–1.35,  
 469 respectively. The  $A$  values of stratiform rainfall were close to those of M48, and the  $b$   
 470 values were close to and smaller than the  $Z$ - $R$  of global stratiform rainfall. Site DLD  
 471 had a similar  $Z$ - $R$  for stratiform rainfall with as M48, while its convective rainfall was  
 472 different from other sites, with a larger  $A$  value (twice as large as other sites) and smaller  
 473  $b$  value, which probably relates to its own local climatic influences formed in a narrow  
 474 valley. In addition, it is clear that the  $A$  value of stratiform rainfall increased from the  
 475 southern slopes to northern slopes, while the opposite was the case for convective  
 476 rainfall. Also, the  $Z$ - $R$  relationships of the same section are more consistent, such as  
 477 those of the interior or the northern slopes, which have distinct geographic  
 478 characteristics.



479

480 Figure 12. The  $A$  and  $b$  values of the  $Z$ - $R$  relationships for (a) stratiform rainfall and (b)  
 481 convective rainfall at six sites. The purple lines in (a) and cyan lines in (b) correspond  
 482 to the global  $Z$ - $R$  model ( $Z = 295R^{1.49}$  for continental stratiform rainfall and  $Z = 278R^{1.54}$   
 483 for convective rainfall, respectively) (Ghada et al., 2018). The cyan lines in (a) represent  
 484 the midlatitude stratiform rainfall  $Z$ - $R$  model ( $Z = 200R^{1.60}$ , Marshall, 1948); and the  
 485 purple lines in (b) represent the convective rainfall  $Z$ - $R$  model ( $Z = 300R^{1.40}$ ) applied to  
 486 operational weather radar (Fulton et al., 1998).

#### 487 4 Discussion

488 The paper analyses the statistical characteristics of DSD at different sites in the  
 489 Qilian Mountains during the rainy season, which not only contain rainfall classes and  
 490 rainfall types but more importantly reflect the differences between different sites. The  
 491 results from different aspects can be mutually confirmed and have a good representation  
 492 of the spatial distribution, serving as a strong factual basis for discussion of the  
 493 microphysical structure of precipitation. For example, with the rain rate class rising, the  
 494 number concentration of all size bins is increased and the width of DSDs became wider,  
 495 which manifested as convective rainfall having a larger rain rate. In spatial terms, the  
 496 characteristics of precipitation in the interior of the mountains and on the southern  
 497 slopes were closer, whether considering the overall DSD distribution or the  
 498 distributions of DSD parameters. However, there were obvious variabilities at the  
 499 interior sites for DSD parameters due to the influences of local dynamics and thermal  
 500 effects. On the other hand, these characteristics also exhibited some differences between  
 501 the interior and eastern sections of the Qilian Mountains, especially in the discussion of  
 502 DSD parameters for rainfall classes and rainfall types (s Figures 5 and 10). This spatial  
 503 variation in DSD suggests that microphysical processes involved in the DSD are  
 504 influenced by complex topography (altitude, mountain alignment) and potentially  
 505 related to the source of water vapor, development of precipitation process and  
 506 anthropogenic factors.

507 Compared to previous studies that focused on eastern [3.48 for  $\log_{10}N_w$  and 1.23  
 508 mm for  $D_m$ , Pu et al.(2020)], southern [3.86 for  $\log_{10}N_w$  and 1.47 mm for  $D_m$ , Zhang et  
 509 al.(2019)], northern [3.60 for  $\log_{10}N_w$  and 1.15 mm for  $D_m$ , Ma et al.(2019b)] and central  
 510 [3.48 for  $\log_{10}N_w$  and 1.54 mm for  $D_m$ , Fu et al.(2020)] China as well the Tibetan  
 511 Plateau[3.47 for  $\log_{10}N_w$  and 1.05 mm for  $D_m$ , Wang et al.(2021)], the Qilian Mountains  
 512 region has its own unique DSD characteristics and  $Z$ - $R$  relationship during the rainy  
 513 season, including a smaller raindrop diameter with a higher number concentration [3.69  
 514 for  $\log_{10}N_w$  and 0.94 mm for  $D_m$ ]. Moreover, the division of rainfall rate classes in the

515 Qilian Mountains more adequately reflects the DSD characteristics in each class, unlike  
516 when using the classification method of other sites with larger rainfall rates. More  
517 importantly, the proposed classification of stratiform and convective rainfall can clearly  
518 distinguish between the distribution of  $\log_{10}N_w$  versus  $D_m$  in different rainfall types, for  
519 which the dividing line (slope of  $-1.6$  and intercept of  $6.008$ ) between stratiform and  
520 convective rainfall has the same slope as the line (slope of  $-1.6$  and intercept of  $6.3$ )  
521 given by Bringi et al (2003). Furthermore, according to this method, it can be proven  
522 that convective events are not belong to the continental-like cluster or maritime-like  
523 cluster, conforming to the unique precipitation characteristics of the Qilian Mountains.

524 As mentioned above, the characteristics of DSD mainly describe diameters larger  
525 than  $0.2$  mm, which is limited by the observation instruments being unable to detect  
526 small drops of diameter less than  $0.2$  mm. Therefore, it is not a complete DSD, and the  
527 number concentration of small drops of diameter less than  $0.5$  mm is underestimated.  
528 Recent studies have been devoted to improving DSD observations in order to overcome  
529 the limitations of disdrometers. A study by Thurai et al. (2017) obtained a more  
530 complete DSD by splicing 2DVD and MPS (Meteorological Particle Spectrometer)  
531 measurements to observe DSDs and developed a technology to reconstruct the drizzle-  
532 mode DSD (Raupach et al., 2019), which a good presentation of the DSD of small  
533 raindrops was provided, and important applications were highlighted.

## 534 **5 Summary and conclusion**

535 Based on six months of DSD data observed over the southern slopes, northern  
536 slopes and interior of the Qilian Mountains, the characteristics and differences of DSD  
537 were studied, and the  $Z-R$  relationships of six sites were discussed. The main  
538 conclusions can be summarized as follows:

539

- 540 1. For all rainfall events, the number concentrations of small and large raindrops in  
541 the interior and on the southern slopes were greater than that on the northern slopes,  
542 while midsize raindrops were less. The DSD of the interior of the mountains  
543 showed great variability, mainly in terms of the  $\log_{10}N_w$  and  $D_m$  (DSD parameters),  
544 which was quite different to the case for the northern slopes.
- 545 2. The rainfall rates were divided into six categories based on the DSD characteristics:  
546 C1,  $R < 0.5$ ; C2,  $0.5 \leq R < 2$ ; C3,  $2 \leq R < 4$ ; C4,  $4 \leq R < 6$ ; C5,  $6 \leq R < 10$ ; and C6,  $> 10$   
547  $\text{mm h}^{-1}$ . As the rainfall rate increased, the differences in number concentration of  
548 each raindrop size became significantly larger, especially at the interior sites.  
549 Besides, classes C5 and C6 made a relatively large contribution to the northern  
550 slopes, with a greater probability of heavy precipitation events.
- 551 3. The dispersion degree of  $\log_{10}N_w$  and  $D_m$  at the six sites was  $8.3\%$  and  $10.0\%$  for  
552 stratiform rainfall and  $10.4\%$  and  $23.4\%$  for convective rainfall, respectively. It is  
553 easier to increase the number concentration of large raindrops in the interior area  
554 of the mountains during convective rainfall. Meanwhile, there is a greater increase  
555 in the number concentration of raindrops over the northern slopes during  
556 convective rainfall.
- 557 4. The dispersion degree of coefficient  $A$  and exponent  $b$  in the  $Z-R$  relationship for

558 the six sites was 42.5% and 10.7%, respectively. Overall, the  $Z$ - $R$  relationships of  
559 the ipsilateral sites were more consistent; and the  $A$  value of stratiform rainfall  
560 increased from the southern slopes to northern slopes, while the opposite was true  
561 for convective rainfall. The  $Z$ - $R$  relationships in stratiform rainfall were similar  
562 and generally underestimated by the  $Z=200R^{1.6}$  model used for midlatitude  
563 stratiform rainfall; and the  $Z$ - $R$  relationships for convective precipitation varied  
564 greatly at different sites, which were overestimated by  $Z=300R^{1.4}$  at lower rain  
565 rates values and underestimated at higher rain rates values.

566 This study reveals the microphysical variability of precipitation over the complex  
567 topography of the arid and semi-arid regions of Northwest China, which can not only  
568 improve local numerical simulations, but also provides a basis for further understanding  
569 the differences in DSD characteristics formed at the mesoscale due to topographic  
570 factors and the water vapor distribution, etc. This study holds importance as a basis for  
571 the future implementation of weather modification techniques, which is of great  
572 significance in solving the shortage of water resources in the arid and semi-arid regions.

573 *Data availability.* Disdrometer data used in this study are available by contacting the  
574 authors.

575 *Author contributions.* WM conducted the detailed analysis; WZ provided financial  
576 support and conceived the idea; MK collated the observation data; all the authors  
577 contributed to the writing and revisions.

578 *Competing interests.* The authors declare that they have no conflict of interest.

## 579 **Acknowledgments**

580 The work was supported by Weather modification ability construction project of  
581 Northwest China under grant No. ZQC-R18208 and The Second Tibetan Plateau  
582 Comprehensive Scientific Expedition Grant No. 2019QZKK0104. Thanks are given to  
583 Asi Zhang for her help in discussing some questions. The authors also thank reviewers  
584 and editors for their helpful suggestion for this study

585 **References**

- 586 Adirosi, E., N. Roberto, M. Montopoli, E. Gorgucci, and L. Baldini, 2018: Influence of  
587 disdrometer type on weather radar algorithms from measured DSD: Application  
588 to Italian climatology. *Atmosphere*, 9, 360.
- 589 Angulo-Martínez, M., and A. Barros, 2015: Measurement uncertainty in rainfall kinetic  
590 energy and intensity relationships for soil erosion studies: An evaluation using  
591 PARSIVEL disdrometers in the Southern Appalachian Mountains.  
592 *Geomorphology*, 228, 28-40.
- 593 Atlas, D., R. Srivastava, and R. S. Sekhon, 1973: Doppler radar characteristics of  
594 precipitation at vertical incidence. *Reviews of Geophysics*, 11, 1-35.
- 595 Bringi, V., V. Chandrasekar, J. Hubbert, E. Gorgucci, W. Randeu, and M. Schoenhuber,  
596 2003: Raindrop size distribution in different climatic regimes from disdrometer  
597 and dual-polarized radar analysis. *Journal of the atmospheric sciences*, 60, 354-  
598 365.
- 599 Campos, E., I. Zawadzki, M. Petitdidier, and W. Fernandez, 2006: Measurement of  
600 raindrop size distributions in tropical rain at Costa Rica. *Journal of Hydrology*,  
601 328, 98-109.
- 602 Chen, B., J. Yang, and J. Pu, 2013: Statistical characteristics of raindrop size  
603 distribution in the Meiyu season observed in eastern China. *Journal of the*  
604 *Meteorological Society of Japan. Ser. II*, 91, 215-227.
- 605 Dolan, B., B. Fuchs, S. Rutledge, E. Barnes, and E. Thompson, 2018: Primary modes  
606 of global drop size distributions. *Journal of the Atmospheric Sciences*, 75, 1453-  
607 1476.
- 608 Das, S., and A. Maitra, 2018: Characterization of tropical precipitation using drop size  
609 distribution and rain rate-radar reflectivity relation. *Theoretical and applied*  
610 *climatology*, 132, 275-286.
- 611 Fu, Z., and Coauthors, 2020: Statistical characteristics of raindrop size distributions and  
612 parameters in Central China during the Meiyu seasons. *Journal of Geophysical*  
613 *Research: Atmospheres*, 125, e2019JD031954.
- 614 Fulton, R. A., J. P. Breidenbach, D.-J. Seo, D. A. Miller, and T. O'Bannon, 1998: The  
615 WSR-88D rainfall algorithm. *Weather and forecasting*, 13, 377-395.
- 616 Geoffroy, O., A. Siebesma, and F. Burnet, 2014: Characteristics of the raindrop  
617 distributions in RICO shallow cumulus. *Atmospheric Chemistry and Physics*, 14,  
618 10897-10909.
- 619 Ghada, W., A. Buras, M. Lüpke, C. Schunk, and A. Menzel, 2018: Rain microstructure  
620 parameters vary with large-scale weather conditions in Lausanne, Switzerland.  
621 *Remote Sensing*, 10, 811.
- 622 Giannetti, F., and Coauthors, 2017: Real-time rain rate evaluation via satellite downlink  
623 signal attenuation measurement. *Sensors*, 17, 1864.
- 624 Gou, X., F. Chen, M. Yang, J. Li, J. Peng, and L. Jin, 2005: Climatic response of thick  
625 leaf spruce (*Picea crassifolia*) tree-ring width at different elevations over Qilian  
626 Mountains, northwestern China. *Journal of Arid Environments*, 61, 513-524.

627 Guyot, A., Pudashine, J., Protat, A., Uijlenhoet, R., Pauwels, V., Seed, A., and Walker,  
628 J. P., 2019: Effect of disdrometer type on rain drop size distribution  
629 characterisation: A new dataset for south-eastern Australia. *Hydrology and Earth  
630 System Sciences*, 23, 4737-4761.

631 Jash, D., E. Resmi, C. Unnikrishnan, R. Sumesh, T. Sreekanth, N. Sukumar, and K.  
632 Ramachandran, 2019: Variation in rain drop size distribution and rain integral  
633 parameters during southwest monsoon over a tropical station: An inter-comparison  
634 of disdrometer and Micro Rain Radar. *Atmospheric Research*, 217, 24-36.

635 Jaffrain, J., and Berne, A., 2011: Experimental quantification of the sampling  
636 uncertainty associated with measurements from PARSIVEL disdrometers. *Journal  
637 of Hydrometeorology*, 12, 352-370.

638 Kruger, A., and W. F. Krajewski, 2002: Two-dimensional video disdrometer: A  
639 description. *Journal of Atmospheric and Oceanic Technology*, 19, 602-617.

640 Le Loh, J., D.-I. Lee, and C.-H. You, 2019: Inter-comparison of DSDs between  
641 Jincheon and Miryang at South Korea. *Atmospheric Research*, 227, 52-65.

642 Li, Z., and Coauthors, 2019: Climate background, relative rate, and runoff effect of  
643 multiphase water transformation in Qilian Mountains, the third pole region.  
644 *Science of The Total Environment*, 663, 315-328.

645 Lim, Y. S., J. K. Kim, J. W. Kim, B. I. Park, and M. S. Kim, 2015: Analysis of the  
646 relationship between the kinetic energy and intensity of rainfall in Daejeon, Korea.  
647 *Quaternary International*, 384, 107-117.

648 Ma, L., L. Zhao, D. Yang, Y. Xiao, L. Zhang, and Y. Qiao, 2019a: Analysis of Raindrop  
649 Size Distribution Characteristics in Permafrost Regions of the Qinghai–Tibet  
650 Plateau Based on New Quality Control Scheme. *Water*, 11, 2265.

651 Ma, Y., G. Ni, C. V. Chandra, F. Tian, and H. Chen, 2019b: Statistical characteristics of  
652 raindrop size distribution during rainy seasons in the Beijing urban area and  
653 implications for radar rainfall estimation. *Hydrology and Earth System Sciences*,  
654 23, 4153-4170.

655 Marshall, J. S., 1948: The distribution of raindrops with size. *J. meteor.*, 5, 165-166.

656 McFarquhar, G. M., T.-L. Hsieh, M. Freer, J. Mascio, and B. F. Jewett, 2015: The  
657 characterization of ice hydrometeor gamma size distributions as volumes in  $N_0$ –  
658  $\lambda$ – $\mu$  phase space: Implications for microphysical process modeling. *Journal of  
659 Atmospheric Sciences*, 72, 892-909.

660 Narayana Rao, T., N. Kirankumar, B. Radhakrishna, and D. Narayana Rao, 2006: On  
661 the variability of the shape-slope parameter relations of the gamma raindrop size  
662 distribution model. *Geophysical research letters*, 33.

663 Protat, A., and Coauthors, 2019: The latitudinal variability of oceanic rainfall properties  
664 and its implication for satellite retrievals: 1. Drop size distribution properties.  
665 *Journal of Geophysical Research: Atmospheres*, 124, 13291-13311.

666 Pu, K., X. Liu, Y. Wu, S. Hu, L. Liu, and T. Gao, 2020: A comparison study  
667 of raindrop size distribution among five sites at the urban scale during the  
668 East Asian rainy season. *Journal of Hydrology*, 590, 125500, <https://doi.org/>

669 g/10.1016/j.jhydrol.2020.125500.

670 Penide, G., A. Protat, V. V. Kumar, and P. T. May, 2013: Comparison of two  
671 convective/stratiform precipitation classification techniques: Radar reflectivity  
672 texture versus drop size distribution–based approach. *Journal of Atmospheric and*  
673 *Oceanic Technology*, 30, 2788-2797.

674 Qin, Y., H. Lei, D. Yang, B. Gao, Y. Wang, Z. Cong, and W. Fan, 2016: Long-term  
675 change in the depth of seasonally frozen ground and its ecohydrological impacts  
676 in the Qilian Mountains, northeastern Tibetan Plateau. *Journal of Hydrology*, 542,  
677 204-221.

678 Rincon, R. F., and R. H. Lang, 2002: Microwave link dual-wavelength measurements  
679 of path-average attenuation for the estimation of drop size distributions and rainfall.  
680 *IEEE Transactions on geoscience and remote sensing*, 40, 760-770.

681 Raupach, T. H., M. Thurai, V. Bringi, and A. Berne, 2019: Reconstructing the drizzle  
682 mode of the raindrop size distribution using double-moment normalization.  
683 *Journal of Applied Meteorology and Climatology*, 58, 145-164.

684 Seela, B. K., J. Janapati, P. L. Lin, K. K. Reddy, R. Shirooka, and P. K. Wang, 2017: A  
685 comparison study of summer season raindrop size distribution between Palau and  
686 Taiwan, two islands in western Pacific. *Journal of Geophysical Research:*  
687 *Atmospheres*, 122, 11,787-711,805.

688 Smith, J. A., E. Hui, M. Steiner, M. L. Baeck, W. F. Krajewski, and A. A. Ntelekos,  
689 2009: Variability of rainfall rate and raindrop size distributions in heavy rain.  
690 *Water Resources Research*, 45.

691 Thurai, M., P. Gatlin, and V. Bringi, 2016: Separating stratiform and convective rain  
692 types based on the drop size distribution characteristics using 2D video  
693 disdrometer data. *Atmospheric Research*, 169, 416-423.

694 Thurai, M., P. Gatlin, V. Bringi, W. Petersen, P. Kennedy, B. Notaroš, and L. Carey,  
695 2017: Toward completing the raindrop size spectrum: Case studies involving 2D-  
696 video disdrometer, droplet spectrometer, and polarimetric radar measurements.  
697 *Journal of Applied Meteorology and Climatology*, 56, 877-896.

698 Testud, J., S. Oury, R. A. Black, P. Amayenc, and X. Dou, 2001: The concept of  
699 “normalized” distribution to describe raindrop spectra: A tool for cloud physics  
700 and cloud remote sensing. *Journal of Applied Meteorology*, 40, 1118-1140.

701 Tian, H., T. Yang, and Q. Liu, 2014: Climate change and glacier area shrinkage in the  
702 Qilian mountains, China, from 1956 to 2010. *Annals of Glaciology*, 55, 187-197.

703 Tokay A, Wolff D B, Petersen W A, 2014. Evaluation of the New Version of the Laser-  
704 Optical Disdrometer, OTT Parsivel<sup>2</sup>. *Journal of atmospheric and oceanic*  
705 *technology*, 31, 1276-1288.

706 Ulbrich C W., 1983: Natural variations in the analytical form of the raindrop size  
707 distribution. *Journal of climate and applied meteorology*, 22, 1764-1775.

708 Wainwright, C. E., D. T. Dawson, M. Xue, and G. Zhang, 2014: Diagnosing the  
709 intercept parameters of the exponential drop size distributions in a single-moment  
710 microphysics scheme and impact on supercell storm simulations. *Journal of*



711 Applied Meteorology and Climatology, 53, 2072-2090.  
712 Wang, Y., J. Zheng, Z. Cheng, and B. Wang, 2020: Characteristics of Raindrop Size  
713 Distribution on the Eastern Slope of the Tibetan Plateau in Summer. Atmosphere,  
714 11, 562.  
715 Wu, Y., and L. Liu, 2017: Statistical characteristics of raindrop size distribution in the  
716 Tibetan Plateau and southern China. Advances in Atmospheric Sciences, 34, 727-  
717 736.  
718 Yang, L., J. Smith, M. L. Baeck, B. Smith, F. Tian, and D. Niyogi, 2016: Structure and  
719 evolution of flash flood producing storms in a small urban watershed. Journal of  
720 Geophysical Research: Atmospheres, 121, 3139-3152.  
721 Zhang, A., and Coauthors, 2019: Statistical characteristics of raindrop size distribution  
722 in the monsoon season observed in southern China. Remote Sensing, 11, 432.  
723 Zhao, P., and Coauthors, 2019: The Tibetan Plateau surface-atmosphere coupling  
724 system and its weather and climate effects: The Third Tibetan Plateau Atmospheric  
725 Science Experiment. Journal of Meteorological Research, 33, 375-399.  
726 Zeng, Y., and Coauthors, 2021: Statistical Characteristics of Raindrop Size Distribution  
727 during Rainy Seasons in Northwest China. Advances in Meteorology, 2021.  
728